NANO LETTERS
Cite This: Nano Lett. XXXX, XXX, XXX−XXX
Letter
pubs.acs.org/NanoLett

Imaging of Optically Active Defects with Nanometer Resolution

Jiandong Feng,*[,†] Hendrik Deschout,[†] Sabina Caneva,[‡] Stephan Hofmann,[‡] Ivor Lončarić,[§] Predrag Lazić,[§] and Aleksandra Radenovic*[,†]

[†]Laboratory of Nanoscale Biology, Institute of Bioengineering, School of Engineering, École Polytechnique Fédérale de Lausanne (EPFL), 1015 Lausanne, Switzerland

[‡]Department of Engineering, University of Cambridge, JJ Thomson Avenue, CB3 0FA Cambridge, United Kingdom

[§]Institut Ruđer Bošković, Bijenička 54, 10000 Zagreb, Croatia

Supporting Information

ABSTRACT: Point defects significantly influence the optical and electrical properties of solid-state materials due to their interactions with charge carriers, which reduce the band-to-band optical transition energy. There has been a demand for developing direct optical imaging methods that would allow *in situ* characterization of individual defects with nanometer resolution. Here, we demonstrate the localization and quantitative counting of individual optically active defects in monolayer hexagonal boron nitride using single molecule localization microscopy. By exploiting the blinking behavior of defect emitters to temporally isolate multiple emitters within one diffraction limited region, we could resolve two defect emitters with a point-to-point distance down to ten nanometers. The results and conclusion presented in this work add unprecedented dimensions toward future applications of defects in quantum information processing and biological imaging.

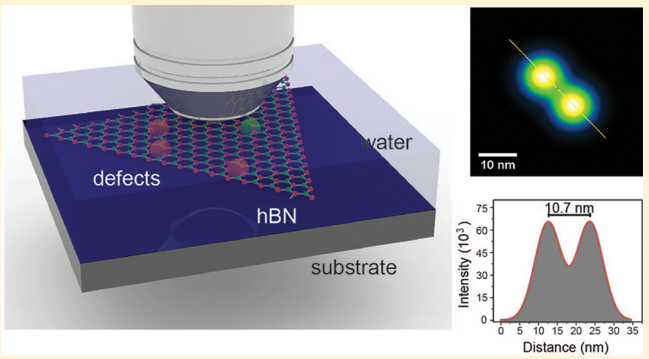

KEYWORDS: *Super resolution microscopy, boron nitride monolayer, point defects, localization microscopy*

Vacancy defects are of crucial importance in determining both transport and optical properties of semiconductors. Through interaction with excitons, defects can be optically active at energies lower than the band-to-band optical transition energy, as revealed in their photoluminescence experiments.[1] Defects in diamond[2] and two-dimensional materials[3] have been demonstrated to be able to serve as single photon emitters, which are essential for quantum-information processing.[4] Due to their extraordinary quantum mechanical properties in sensing the local electromagnetic field and temperature, defects are also considered as promising candidates for biological imaging at the nanoscale.[5] Mapping and localizing individual defects at high spatial resolution will, therefore, add unprecedented dimensions to both applications.

Scanning tunneling microscope (STM) has long been used to directly visualize single defects and their electronic structures. With STM, manipulation of individual point defects can be realized via tip-bias-induced electrochemical reactions.[6] Advances in aberration-corrected transmission electron microscope (TEM) greatly improved the resolution in characterizing individual defects.[7,8] Nevertheless, both methods require special sample preparations and are still not optimal for fast *in situ* operations. Therefore, development of direct optical technology that images individual defects would match the emerging requirements in both quantum information processing and bioimaging. However, the optical detection and control are hampered by the diffraction limit, which can accumulate multiple defect emitters for defective materials. Super-resolution microscopy techniques can, in principle, address these problems. Stimulated emission depletion (STED) microscopy has demonstrated a capability of imaging nitrogen−vacancy (N−V) centers in nanodiamond with a resolution of a few nanometers.[9,10] Single-molecule localization microscopy (SMLM), based on localizing sparse sets of switchable fluorescent molecules,[11,12] has also been used for wide-field parallel imaging of N−V centers in diamond.[13,14]

Recently, 2D materials have been shown to host defects that serve as single photon emitters at cryogenic temperatures for transition metal dichalcogenides[15−18] and room temperature for hexagonal boron nitride (h-BN).[19] In quantum information processing, optically active defects in 2D materials are attractive since inherently they do not require total internal reflection. In addition, optically active defects have high light extraction efficiency, and electrical connections can be easily integrated.[3] Therefore, imaging them with super-resolution techniques is of high significance for the realization of reading large-scale networks. The operation at room temperature, together with the high brightness and contrast and defective nature of h-BN

Received: November 14, 2017
Revised: January 12, 2018
Published: February 2, 2018

DOI: 10.1021/acs.nanolett.7b04819
Nano Lett. XXXX, XXX, XXX−XXX

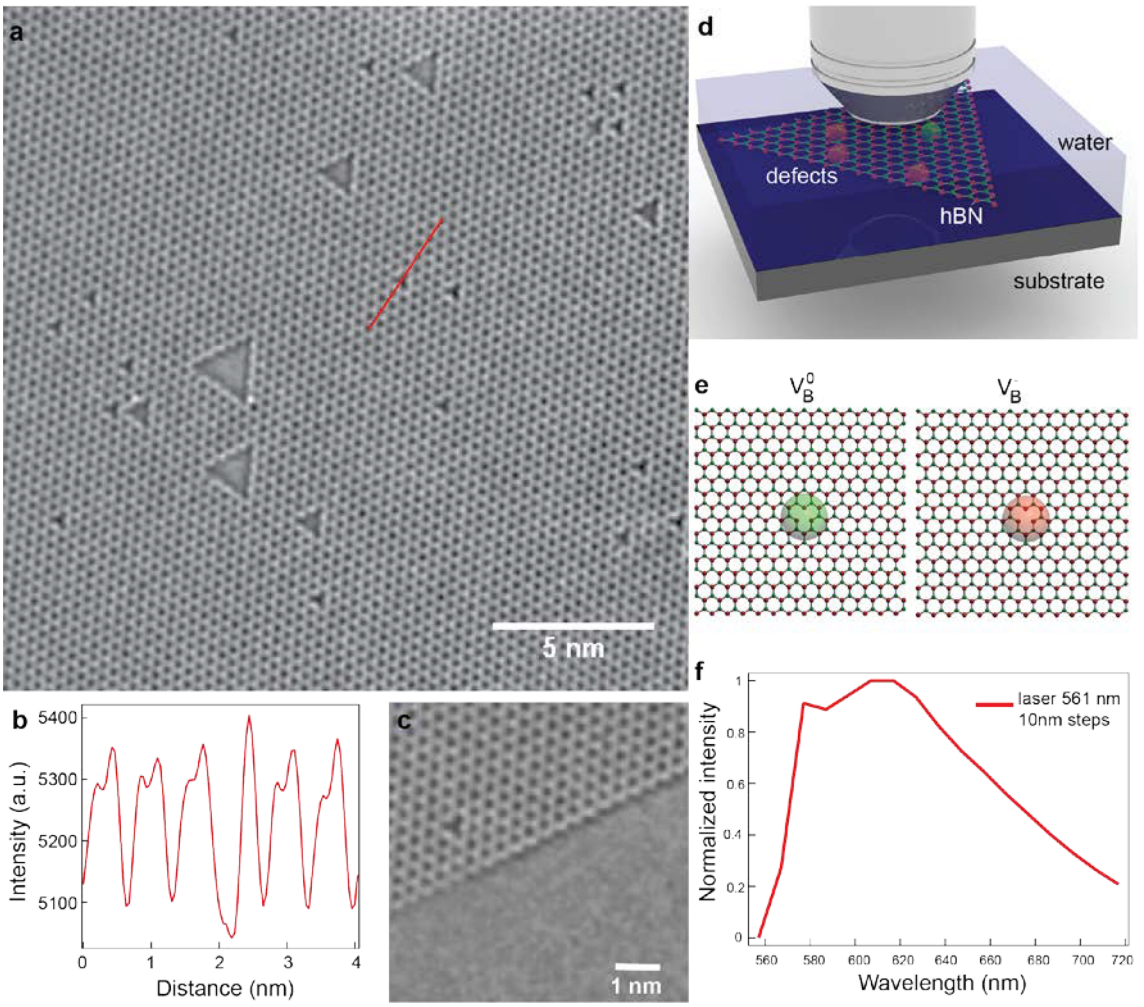

Figure 1. Optically active defects in h-BN. (a) High-resolution TEM imaging of vacancy defects in h-BN. Dominant defects are found to be point defects. (b) Image contrast of the line in panel (a) suggests the defect type to be boron monovacancy. (c) High-resolution TEM imaging of h-BN edges. (d) Schematics of *in situ* characterization of defects in h-BN using SMLM (more details are shown in the Supporting Information methods). (e) Proposed structure of boron monovacancy with neutral and negative charge. (f) Emission spectrum of h-BN defects.

make it the most suitable 2D candidate for room-temperature quantum computing.[3]

Here, we demonstrate the localization and spatial mapping of individual defect emitters in monolayer h-BN by SMLM. This approach allows us to resolve the most precisely localized defect emitters at separations around 10 nm.

Monolayer h-BN comprises alternate boron and nitrogen atoms in a two-dimensional honeycomb arrangement. In order to clarify the structure of atomic defects in h-BN, we first imaged the h-BN samples using aberration-corrected TEM, as shown in Figure 1a. The uniform orientation of all observed defects excludes the possibility of coexistence between boron and nitrogen monovacancies due to the three-fold symmetry of h-BN.[8] Boron monovacancies, further confirmed by the line profile of the image contrast (Figure 1b), are found to be dominant for the h-BN materials.[8] Because of the electron knock-on effect during TEM irradiation coupled with the beam-induced etching with residual water or oxygen present in the system, more defects can be directly introduced and enlarged to triangular pores,[20] as shown in Figure 1a,c.

Photoluminescence experiments on h-BN specimens that were not subjected to electron radiation with TEM suggest that the defects are intrinsic (Figure 1d), which are dependent on growth conditions that may arise during the electrochemical transfer process.[21] Two kinds of emissions are observed in our experiments: the weak homogeneous fluorescence that follows the entire triangular shaped h-BN monolayer[21] and the bright individual emitters. Spectral response from one of the bright emitters is shown in Figure 1f, and we also compared the spectra for both types of emitters in Figure S1. As defect-free monolayer h-BN has a large bandgap (around 5−6 eV), we speculate that two candidates for the observed emission could be either boron or nitrogen monovacancies. Due to the uncertainty in calculating their electronic structure using the density functional calculations,[22,23] both are reasonable candidates for the observed spectrum. Possible causes for this uncertainty are discussed in the Supporting Information (defect electronic band diagram). According to the TEM results (Figure 1a) and considering the relative density, in monolayer h-BN we have detected mostly boron vacancies that may be responsible for the observed optical activity. We infer that the observed weak homogeneous emission is due to the high density of boron monovacancies with neutral charges V_B^0 in h-BN, and the bright emitters are negatively charged boron monovacancies V_B^-, as proposed in Figure 1e. However, probing intrinsic defect structure without introducing more

DOI: 10.1021/acs.nanolett.7b04819
Nano Lett. XXXX, XXX, XXX−XXX

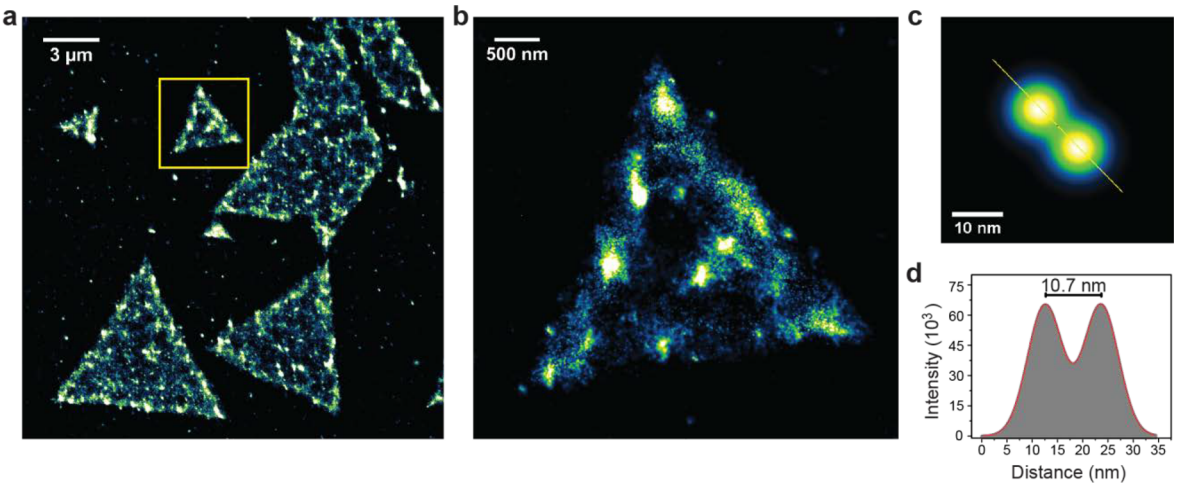

Figure 2. Super-resolution imaging of optically active defects in h-BN. (a) Reconstructed SMLM image of defects in h-BN from an image sequence of 20,000 frames. The imaging condition: DI water and 561 nm laser. Display pixel size: 5 nm. (b) Selected region in panel (a). Display pixel size: 1 nm. (c) With best drift correction achieved with fiducial markers shown in Figure S3, SMLM allows distinguishing two close emitters. (d) Distance profile shown in panel (c) shows a resolving capability of 10.7 nm. The images were rendered as probability maps.

defects with TEM remains a challenge for the current case, which would provide more straightforward correlation. As shown in the emission spectrum Figure 1f, fluorescence emission above 600 nm is mainly coming from V_B^-. We could not avoid the averaging effect in our photoluminescence experiments due to difficulties in isolating individual defects. Better spectroscopic results could be achieved with isolated individual emitters under low-temperature conditions.[23] Other candidates for the observed defect fluorescence can be boron–nitrogen vacancy[19] or three boron plus one nitrogen vacancy. The unique and uniform defect structure of h-BN (Figure 1a) is crucial for the scaling up of a parallel quantum sensor array via selective defect patterning.

Photoswitching was observed after exposure to green light illumination (561 nm). One of the possible explanations for this switching behavior can refer to photoinduced ionization and recombination of defects between its neutral state and charged state.[24] We then verified the wavelength dependence (405, 488, and 561 nm) of defect charge state dynamics and found maximum switching rates at 561 nm. No switching event was observed at 405 nm. The charge conversion process can be understood as V_B^0/V_B^{-1} (or other types of defects) is first excited, and then an electron is captured from conduction band for ionization (V_B^0 to V_B^{-1}) or from valence band for recombination (V_B^{-1} to V_B^0), consistent with the evidence reported for both optical excitation of defect transitions in h-BN[25] and STM measurements on the excited h-BN defects.[26]

This photoswitching behavior sets the playground for optical super-resolution reconstruction, which is based on the temporal isolation of densely packed multiple emitters within one diffraction limited region. SMLM trades temporal resolution for spatial resolution, and therefore, it requires an ideal imaging sample to be spatially fixed and temporally static.[11] Both requirements are fulfilled by the solid-state defective h-BN samples. In addition, in this case, no labeling is involved, and the strong emitters are extremely bright and do not bleach. Direct imaging of the sample itself makes it an ideal test case for achieving the fundamental limit of SMLM resolutions.[11]

Initial image frames typically consisted of dense weak fluorescence background, presumably dominated by the much larger population of defects still in the inactivated state. After initial activation, a lot of asynchronous blinking events between two states were observed. Due to the brightness of solid-state emitters, we achieved a high localization precision[11] from strong emitters. For example, a localization precision of 3.5 nm is obtained for the emitters shown in Figure 2c. Giving an average localization precision is challenging due to the merged broad distribution of weak and bright emitters. Reconstruction by summing up all temporally isolated Gaussian location distributions of individual emitters defined by their coordinates and localization precision yields Figure 2a,b. In contrast, a diffraction limited image is produced by summing all image stacks to overlap their signals (Figure S2).

The ability to distinguish two closest emitters also imposes stringent requirements on stage drift correction. Precise drift correction can be achieved with an active feedback-controlled system[27,28] or postimaging processing method using fiducial markers.[11] We used a large number of fiducial markers to achieve an accurate drift correction. In a representative experiment shown in Figure S3, trajectories of 27 fiducial markers are used to calculate the averaged drift trajectory and remaining drift error after correction. To demonstrate the imaging capability of solid-state SMLM for individual defects, we first employed Fourier ring correlation to estimate the resolution,[29] and we obtained 46 nm (Figure S4). However, in this case, individual emitters, as well as their distinguishability are more relevant instead of revealing the structure itself. As shown in Figure 2c, high localization precision and accurate drift correction allowed distinguishing two neighboring emitters with a separation of 10.7 nm (Figure 2d). We would like to note that the emitters exhibit a broad distribution of their photon counts (Figure S5); thus, this resolving capability is dictated by the photophysics and density of strong emitters. Direct optical imaging also allows for *in situ* characterization of defects under ambient conditions, for example, probing their chemistry and dynamics in different pH environments (Figure S6), surface depositions (Figure S7), and isotopic solvents (Figure S8). Among these conditions, the fluorescence signals were found to be sensitive to the acidity of the environment.

Compared to TEM and STM, for *in situ* operation under ambient conditions, SMLM introduces minimum destruction to the sample. The same argument also holds for the high

DOI: 10.1021/acs.nanolett.7b04819
Nano Lett. XXXX, XXX, XXX−XXX

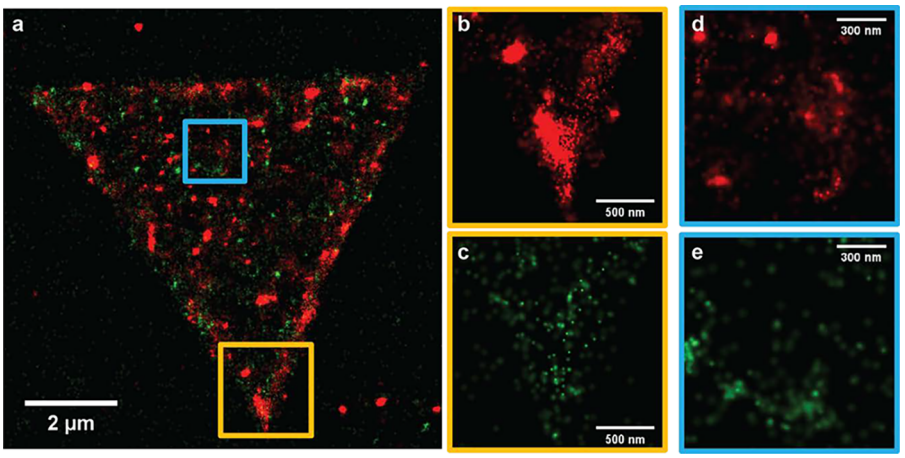

Figure 3. Dual color imaging reveals chemical contrast. (a) Composited dual color super-resolution image of defect emitters in h-BN from image sequence of 20,000 frames. The imaging condition: DI water. Green channel: 488 nm laser. Red channel: 561 nm laser. (b–e) Selected regions in panel (a). The images were rendered as probability maps. Display pixel size: 5 nm.

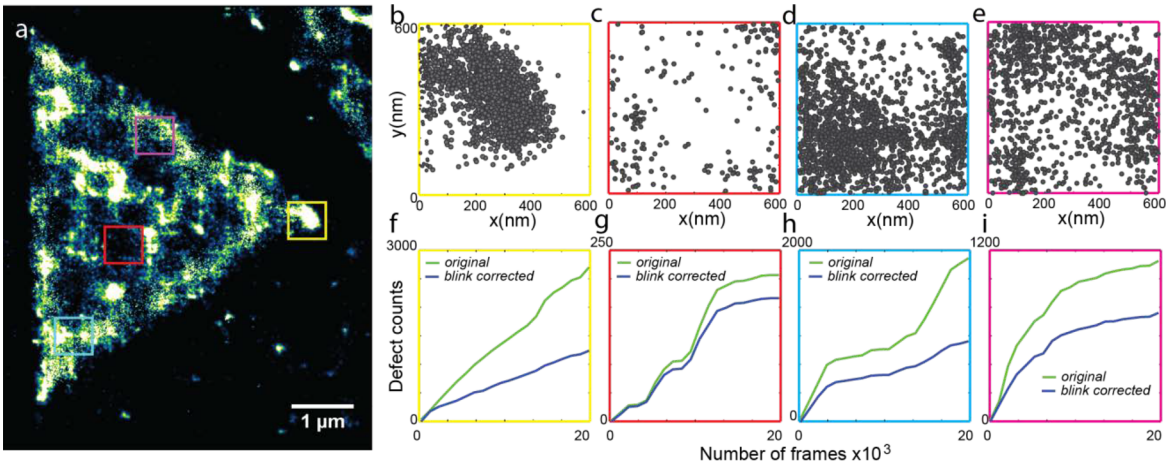

Figure 4. Counting defects in h-BN using quantitative SMLM. (a) Super-resolution imaging and mapping of defect emitters in h-BN with color marked region of interest (ROI). (b–e) Localizations in color marked ROI in panel (a). ROI size: 600 nm × 600 nm. (f–i) Estimation of defect number in panels (b–e) as a function of image frame numbers using total number of localizations (original) and blink correction, respectively. The obtained density: (b) 3268 μm^{-2} (blink corrected) to 7246 μm^{-2} (original); (c) 514 μm^{-2} (blink corrected) to 606 μm^{-2} (original); (d) 2849 μm^{-2} (blink corrected) to 5208 μm^{-2} (original); (e) 2252 μm^{-2} (blink corrected) to 3247 μm^{-2} (original). Imaging condition: DI water and 561 nm laser.

power density used for the depletion laser beam in STED.[9] In addition, standard SMLM has a relatively large field of view, adequate for the imaging of single-crystal 2D material grains. Recently, novel SMLM modalities[30,31] have extended the field of view considerably. The spatial resolution of our results can still be improved using better drift correction methods[28] while a better temporal resolution can be achieved by a spatiotemporal cumulant analysis of the image sequence in super-resolution optical fluctuation imaging (SOFI),[32] shown in Figure S9. SOFI would be particularly interesting for revealing the dynamical processes on defects at the relevant time scales.

Although we are imaging the structure itself without labeling, solid-state SMLM can also provide additional information for revealing chemical contrast of defect types owning to the imaging capability with multiple color channels, as shown in the composited Figure 3a. The dual color imaging led to a preferred spatial distribution of strong emitters near the edge under red channel (Figure 3b,d, laser 561 nm), while no spatial preference was found for green channel (Figure 3c,e, laser 488 nm). This difference could result either from the difference of charge transition rates or defect number and types (see the discussion of possible defect types in the Supporting Information), which was natively formed during growth or transfer.[21] A further determination would require the combination of SMLM with spectroscopic approaches[33] like photoluminescence, deep-level transient spectroscopy, or electron energy-loss spectroscopy. We foresee that such correlative techniques will provide further information on the electronic structures of individual defects.

In addition to chemical contrast, SMLM also offers quantitative information on the number of defects, which can be estimated based on their localizations (Figure 4a and b–e). We also merged the localizations accounting for the localization error.[34] The counting results from strict correction and total localizations offered both the bottom and upper limit of the defect density (Figure 4f–i). Further improvement on this estimation can be made if the photophysics of defect emitters would be clearer. The obtained defect density (3268–7246 μm^{-2} for dense region (Figure 4b) and 514–606 μm^{-2} for sparse region (Figure 4c)) of h-BN is comparable to previous results in ion transport,[35] while quantitative SMLM avoids the averaging effect in ion transport measurements. We also used

DOI: 10.1021/acs.nanolett.7b04819
Nano Lett. XXXX, XXX, XXX–XXX

balanced SOFI (bSOFI) to obtain a density map of the defects as bSOFI (Figure S9) was demonstrated to be more accurate than PALM for high-density emitters.[36] This method provides a quantitative single molecule approach for estimating defect density in semiconductors on large areas.

A further interest to look at the quantum emitters is their spin properties, which can be optically read out when subject to electromagnetic fields, as shown in the measurements with nuclear quadrupole resonance spectroscopy.[37] However, our method also provides a new approach to probe the properties of 2D materials since defects have been proven to perform a crucial role in determining their electrical transport and optical properties. To conclude, we have demonstrated the solid-state SMLM technique for imaging and counting quantum emitters in h-BN with the capability of distinguishing two closest emitters at a few nanometers. The achieved high localization precision may find future applications in semiconductor thin film characterization, quantum information processing, and biological imaging.

■ ASSOCIATED CONTENT

Supporting Information

The Supporting Information is available free of charge on the ACS Publications website at DOI: 10.1021/acs.nanolett.7b04819.

Methods for sample preparation, imaging setup and conditions, and defect electronic band diagram (PDF)

■ AUTHOR INFORMATION

Corresponding Authors

*E-mail: jiandong.feng@epfl.ch.
*E-mail: aleksandra.radenovic@epfl.ch.

ORCID

Stephan Hofmann: 0000-0001-6375-1459
Ivor Lončarić: 0000-0002-5554-4641
Aleksandra Radenovic: 0000-0001-8194-2785

Author Contributions

J.F. conceived the idea and interpreted the results. J.F. wrote the manuscript with inputs from A.R. J.F., H.D., and A.R. designed experiments. J.F. and H.D. performed experiments. H.D. processed all images. S.C. and S.H. performed materials growth. I.L. and P.L. performed DFT calculations. All authors agreed with the final version of the manuscript.

Notes

The authors declare no competing financial interest.

■ ACKNOWLEDGMENTS

This work was financially supported by Swiss National Science Foundation SNSF (200021 153653). We thank the Centre Interdisciplinaire de Microscopie Electronique (CIME) at the École Polytechnique fédérale de Lausanne (EPFL) for access to electron microscopes, Ke Liu, Davide Deiana, and Duncan T. L. Alexander for TEM imaging. Device fabrication was partially carried out at the EPFL Center for Micro/Nanotechnology (CMi). Special thanks to Martina Lihter for hBN transfer and Tomas Lukes for bSOFI image analysis of which results are given in Figure S9. The work performed in Cambridge was supported by the EPSRC Cambridge NanoDTC, EP/L015978/1. I. L. and P. L. were supported by the Unity Through Knowledge Fund, Contract No. 22/15 and H2020 CSA Twinning Project No. 692194, RBI-T-WINNING.

■ REFERENCES

(1) Tongay, S.; Suh, J.; Ataca, C.; Fan, W.; Luce, A.; Kang, J. S.; Liu, J.; Ko, C.; Raghunathanan, R.; Zhou, J. *Sci. Rep.* **2013**, *3*, 2657.
(2) Kurtsiefer, C.; Mayer, S.; Zarda, P.; Weinfurter, H. *Phys. Rev. Lett.* **2000**, *85* (2), 290.
(3) Aharonovich, I.; Englund, D.; Toth, M. *Nat. Photonics* **2016**, *10* (10), 631−641.
(4) Pan, J.-W.; Chen, Z.-B.; Lu, C.-Y.; Weinfurter, H.; Zeilinger, A.; Żukowski, M. *Rev. Mod. Phys.* **2012**, *84* (2), 777.
(5) Schirhagl, R.; Chang, K.; Loretz, M.; Degen, C. L. *Annu. Rev. Phys. Chem.* **2014**, *65*, 83−105.
(6) Wong, D.; Velasco, J., Jr; Ju, L.; Lee, J.; Kahn, S.; Tsai, H.-Z.; Germany, C.; Taniguchi, T.; Watanabe, K.; Zettl, A. *Nat. Nanotechnol.* **2015**, *10* (11), 949−953.
(7) Hashimoto, A.; Suenaga, K.; Gloter, A.; Urita, K.; Iijima, S. *Nature* **2004**, *430* (7002), 870−873.
(8) Jin, C.; Lin, F.; Suenaga, K.; Iijima, S. *Phys. Rev. Lett.* **2009**, *102* (19), 195505.
(9) Rittweger, E.; Han, K. Y.; Irvine, S. E.; Eggeling, C.; Hell, S. W. *Nat. Photonics* **2009**, *3* (3), 144−147.
(10) Arroyo-Camejo, S.; Adam, M.-P.; Besbes, M.; Hugonin, J.-P.; Jacques, V.; Greffet, J.-J.; Roch, J.-F.; Hell, S. W.; Treussart, F. *ACS Nano* **2013**, *7* (12), 10912−10919.
(11) Betzig, E.; Patterson, G. H.; Sougrat, R.; Lindwasser, O. W.; Olenych, S.; Bonifacino, J. S.; Davidson, M. W.; Lippincott-Schwartz, J.; Hess, H. F. *Science* **2006**, *313* (5793), 1642−1645.
(12) Rust, M. J.; Bates, M.; Zhuang, X. *Nat. Methods* **2006**, *3* (10), 793−796.
(13) Gu, M.; Cao, Y.; Castelletto, S.; Kouskousis, B.; Li, X. *Opt. Express* **2013**, *21* (15), 17639−17646.
(14) Pfender, M.; Aslam, N.; Waldherr, G.; Neumann, P.; Wrachtrup, J. *Proc. Natl. Acad. Sci. U. S. A.* **2014**, *111* (41), 14669−14674.
(15) He, Y.-M.; Clark, G.; Schaibley, J. R.; He, Y.; Chen, M.-C.; Wei, Y.-J.; Ding, X.; Zhang, Q.; Yao, W.; Xu, X. *Nat. Nanotechnol.* **2015**, *10* (6), 497−502.
(16) Chakraborty, C.; Kinnischtzke, L.; Goodfellow, K. M.; Beams, R.; Vamivakas, A. N. *Nat. Nanotechnol.* **2015**, *10* (6), 507−511.
(17) Koperski, M.; Nogajewski, K.; Arora, A.; Cherkez, V.; Mallet, P.; Veuillen, J.-Y.; Marcus, J.; Kossacki, P.; Potemski, M. *Nat. Nanotechnol.* **2015**, *10* (6), 503−506.
(18) Srivastava, A.; Sidler, M.; Allain, A. V.; Lembke, D. S.; Kis, A.; Imamoğlu, A. *Nat. Nanotechnol.* **2015**, *10* (6), 491−496.
(19) Tran, T. T.; Bray, K.; Ford, M. J.; Toth, M.; Aharonovich, I. *Nat. Nanotechnol.* **2016**, *11* (1), 37−41.
(20) Meyer, J. C.; Chuvilin, A.; Algara-Siller, G.; Biskupek, J.; Kaiser, U. *Nano Lett.* **2009**, *9* (7), 2683−2689.
(21) Caneva, S.; Weatherup, R. S.; Bayer, B. C.; Brennan, B.; Spencer, S. J.; Mingard, K.; Cabrero-Vilatela, A.; Baehtz, C.; Pollard, A. J.; Hofmann, S. *Nano Lett.* **2015**, *15* (3), 1867−1875.
(22) Attaccalite, C.; Bockstedte, M.; Marini, A.; Rubio, A.; Wirtz, L. *Phys. Rev. B: Condens. Matter Mater. Phys.* **2011**, *83* (14), 144115.
(23) Li, X.; Shepard, G. D.; Cupo, A.; Camporeale, N.; Shayan, K.; Luo, Y.; Meunier, V.; Strauf, S. *ACS Nano* **2017**, *11* (7), 6652−6660.
(24) Aslam, N.; Waldherr, G.; Neumann, P.; Jelezko, F.; Wrachtrup, J. *New J. Phys.* **2013**, *15* (1), 013064.
(25) Ju, L.; Velasco, J., Jr; Huang, E.; Kahn, S.; Nosiglia, C.; Tsai, H.-Z.; Yang, W.; Taniguchi, T.; Watanabe, K.; Zhang, Y. *Nat. Nanotechnol.* **2014**, *9* (5), 348−352.
(26) Velasco, J., Jr; Ju, L.; Wong, D.; Kahn, S.; Lee, J.; Tsai, H.-Z.; Germany, C.; Wickenburg, S.; Lu, J.; Taniguchi, T. *Nano Lett.* **2016**, *16* (3), 1620−1625.
(27) Carter, A. R.; King, G. M.; Ulrich, T. A.; Halsey, W.; Alchenberger, D.; Perkins, T. T. *Appl. Opt.* **2007**, *46* (3), 421−427.
(28) Pertsinidis, A.; Zhang, Y.; Chu, S. *Nature* **2010**, *466* (7306), 647−651.
(29) Nieuwenhuizen, R. P.; Lidke, K. A.; Bates, M.; Puig, D. L.; Grünwald, D.; Stallinga, S.; Rieger, B. *Nat. Methods* **2013**, *10* (6), 557−562.

DOI: 10.1021/acs.nanolett.7b04819
Nano Lett. XXXX, XXX, XXX−XXX

(30) Diekmann, R.; Helle, O. I.; Oie, C. I.; McCourt, P.; Huser, T. R.; Schuttpelz, M.; Ahluwalia, B. S. *Nat. Photonics* **2017**, *11* (5), 322−328.
(31) Douglass, K. M.; Sieben, C.; Archetti, A.; Lambert, A.; Manley, S. *Nat. Photonics* **2016**, *10* (11), 705−708.
(32) Dertinger, T.; Colyer, R.; Iyer, G.; Weiss, S.; Enderlein, J. *Proc. Natl. Acad. Sci. U. S. A.* **2009**, *106* (52), 22287−22292.
(33) Zhang, Z.; Kenny, S. J.; Hauser, M.; Li, W.; Xu, K. *Nat. Methods* **2015**, *12* (10), 935−938.
(34) Annibale, P.; Vanni, S.; Scarselli, M.; Rothlisberger, U.; Radenovic, A. *PLoS One* **2011**, *6* (7), e22678.
(35) Walker, M. I.; Ubych, K.; Saraswat, V.; Chalklen, E. A.; Braeuninger-Weimer, P.; Caneva, S.; Weatherup, R. S.; Hofmann, S.; Keyser, U. F. *ACS Nano* **2017**, *11* (2), 1340−1346.
(36) Geissbuehler, S.; Bocchio, N. L.; Dellagiacoma, C.; Berclaz, C.; Leutenegger, M.; Lasser, T. *Opt Nanoscopy* **2012**, *1* (1), 4.
(37) Lovchinsky, I.; Sanchez-Yamagishi, J.; Urbach, E.; Choi, S.; Fang, S.; Andersen, T.; Watanabe, K.; Taniguchi, T.; Bylinskii, A.; Kaxiras, E. *Science* **2017**, *355* (6324), 503−507.

DOI: 10.1021/acs.nanolett.7b04819
Nano Lett. XXXX, XXX, XXX−XXX